Stable Cycling with Intimate Contacts Enabled by Crystallinity-controlled PTFE-based Solvent-free Cathodes in All-solid-state Batteries

Dongsoo Lee and Arumugam Manthiram*

Materials Science and Engineering Program & Texas Materials Institute
The University of Texas at Austin, Austin, TX, 78712-1591 USA

*Corresponding Author
E-mail: rmanth@mail.utexas.edu

Keywords: all-solid-state batteries, solvent-free cathode, polytetrafluoroethylene, sulfide solid electrolyte, cathode-electrolyte interface

Abstract

All-solid-state batteries (ASSBs) employing Li-metal anodes and inorganic solid electrolytes are attracting great attention due to high safety and energy density for next-generation energy storage devices. However, the volume change of cathode active materials can cause contact loss, resulting in charge carrier isolation, heterogeneous current distribution, and poor electrochemical properties in ASSBs. Here, we report a simple, yet effective, solvent-free electrode engineering approach with polytetrafluoroethylene (PTFE) as a binder for ASSBs, enabling intimate contact and stable interfaces with the cathode. We substantiate that the crystallinity of PTFE can be controlled depending on the heat history, and highly crystalline PTFE display robust mechanical properties. High-nickel $LiNi_{0.8}Mn_{0.1}Co_{0.1}O_2$ cathode prepared with crystalline PTFE show improved cycle and rate performances in ASSBs. In addition, it is revealed that the intimate contact between cathode particles with a stable cathode electrolyte (CEI) layer is maintained during cycling by postmortem studies. This simple engineering method can be applied to prepare cathodes with a variety of active materials and solid electrolytes in ASSBs.

1. Introduction

All-solid-state Li batteries (ASSBs) employing a solid electrolyte (SE) and a Li-metal anode provide the potential to meet the requirements for high energy density and safety.[1] With the development of highly conductive inorganic SEs, such as $Li_{10}GeP_2S_{12}$, Li_6PS_5Cl, and $Li_{6.6}Si_{0.6}Sb_{0.5}S_5I$, the bottleneck is no longer the low Li^+ transport of SEs.[2] In addition, inorganic SEs are regarded as single-ion conductors, which would not lead to a dynamic deviation of Li^+ concentration across the cell in ASSBs.[3] However, sulfide-based SEs have an intrinsic disadvantage to restrict their application due to the narrow electrochemical stability window.[4] Furthermore, the existing slurry and electrode preparation method suffers from several disadvantages, such as the use of toxic organic solvents, high processing cost, and degradation of Li^+ conductivities of SEs.[5] To overcome these drawbacks, solvent-free dry electrode processing as well as interfacial protective layers are expected to be a promising strategy to commercialize ASSBs.

The undesirable reaction at the interfaces between cathode active materials (CAMs) and sulfide-based SEs is one of the major issues, resulting in poor electrochemical properties of ASSBs.[6] Generally, oxide anions in CAMs attract Li^+ electrostatically stronger than sulfide anions, forming a resistive interfacial layer at the interfaces.[7] To suppress the interfacial resistance layer, a protective coating layer on the cathodes has been explored with robust materials, such as $LiNbO_3$, Al_2O_3, and Li_2ZrO_3 for ASSBs.[8] Furthermore, although the relatively soft mechanical property of sulfide-based SEs is beneficial for densifying and making close contacts between CAMs and SEs by simple cold pressing (> 300 MPa), the porosity of cathodes is not in an ideal close-packing configuration.[9] Therefore, the slight volumetric strain of CAMs during cycling can cause a loss of contact between CAMs and SEs, resulting in poor electrochemical performances with discontinuous pathways for Li^+ and e^- as well as heterogeneous interfacial reactions.

Furthermore, owing to the chemically reactive feature of sulfide-based SEs, polar solvents cannot be utilized, which makes it difficult to find an appropriate binder and solvent for the manufacturing of slurry-based electrodes.[10] Polytetrafluoroethylene (PTFE) is a widely used material in the industry due to its unique properties, such as high thermal stability, good mechanical stability, and chemical inertness.[11] Moreover, PTFE powder can be easily fibrilized by kneading and electrochemically stable to high voltages.[12] In this regard, free-standing, solvent-free cathodes prepared with PTFE as a binder are widely used in ASSBs to avoid undesirable reactions between CAMs and SEs during the electrode preparation process.[13] However, studies on the electrochemical properties of ASSBs according to the physicochemical properties of PTFE have been overlooked. PTFE is one of the representative semi-crystalline polymers and is composed of a rigid crystalline phase and a soft amorphous phase.[14] The degree of crystallinity of PTFE can be varied by the heating history. Inspired by this point, we focus on solvent-free cathodes prepared with PTFE having different crystallinity, for the first time in ASSBs.

Here, we report a simple, yet effective, engineering approach to enable intimate contacts and stable interfaces of cathodes with the high-nickel $LiNi_{0.8}Mn_{0.1}Co_{0.1}O_2$ (NMC) as a CAM, Li_6PS_5Cl (LPSCl) as a SE, and PTFE as a binder in ASSBs. The degree of crystallinity of PTFE could be easily controlled with different cooling rates (2 and 15 °C min^{-1}) after heating at 200 °C for 10 min. At a higher cooling rate, the degree of crystallinity of PTFE decreases due to the freezing of polymer microstructure before packing into an organized structure. The crystalline PTFE can help to maintain intimate contact between NMC and LPSCl particles in cathodes. NMC cathodes with the semi-crystalline and high crystalline PTFE (hereafter referred to, respectively, as SCP–NMC and CP–NMC) show improved cycle and rate performances compared to the NMC cathode with amorphous PTFE (hereafter referred to as

AP–NMC) with a high areal capacity of 4 mAh cm^{-2}. Especially, CP–NMC shows steady cycling up to 200 cycles with high capacity retention (> 80 %). Furthermore, it is proved that the initially formed cathode electrolyte interphase (CEI) layer between NMC and LPSCl can restrict further decomposition of SEs with an intimate contact of the cathode, as revealed by electrochemical impedance spectroscopy (EIS) studies and X-ray photoelectron spectroscopy (XPS).

2. Results and discussion

In a molecular chain of PTFE, fluorine atoms surround the carbon backbone where the fluorine sheath and the carbon backbone are strongly tied via a C-F bond which has a high bonding energy of 485 kJ mol^{-1} compared to that of a C-H bond (348 kJ mol^{-1}).[15] The configuration is the fundamental reason why PTFE is one of the most stable polymers. PTFE has four different crystalline phases depending on the temperature and pressure, as illustrated in the phase diagram (**Figure 1a**).[16] Under high pressure, PTFE molecules exist in the form of a planar zigzag conformation. At ambient pressure, three different structures exist depending on the temperature. PTFE has a pseudohexagonal structure (phase I) above 30 °C and a triclinic structure (phase II) below 19 °C.[17] In this study, we focused only on phase IV, a hexagonal structure that exists between 19 °C and 30 °C, and all electrochemical characterizations were conducted at room temperature. The individual molecular chains in phase IV adopt a helical structure in which 15 CF_2 units are arranged in 7 turns around the molecular axis (15/7 conformation). **Figure 1b** presents the repeating distance of 1.95 nm along the molecular axis and a separation distance of 0.566 nm between adjacent chains. These values correspond to the phase IV hexagonal system lattice parameters.[18]

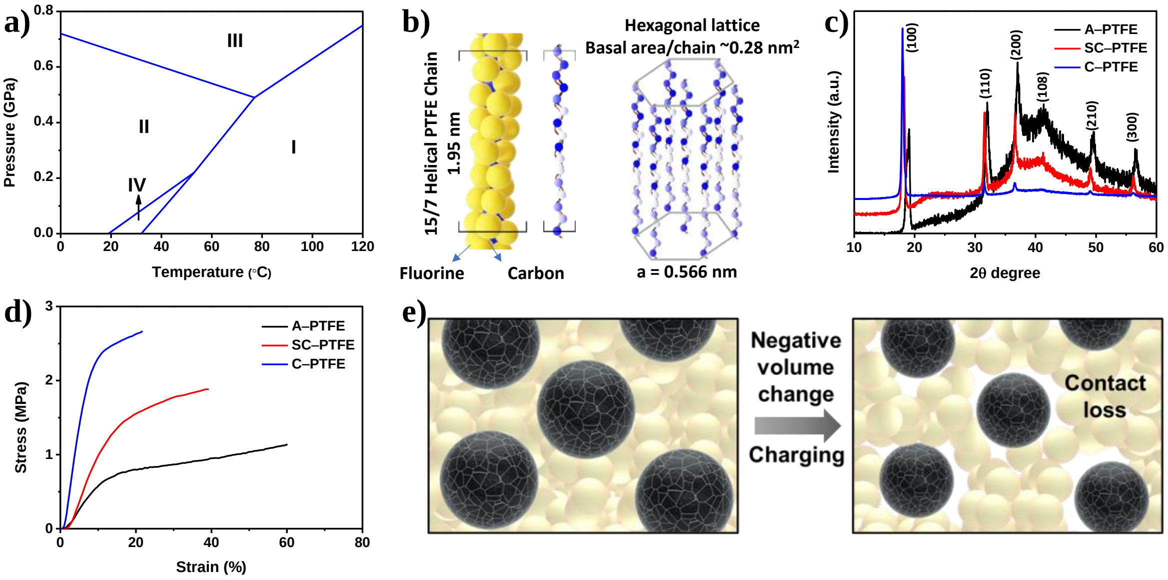

Figure 1. (a) Phase diagram of PTFE. (b) A short-range helical structure and long-range hexagonal packing structure of phase IV crystalline PTFE. (c) XRD patterns and (d) stress-strain curves of A-PTFE, SC-PTFE, and C-PTFE. (e) Schematic illustration of the contact loss of cathode during charging in ASSBs in which CAMs and SEs are expressed in black and yellow, respectively.

PTFE is a semi-crystalline polymer separated by crystalline domains and amorphous regions. Therefore, the mechanical properties and deformation behaviors of PTFE are dependent on the degree of crystallinity.[19] To figure out the crystallographic properties of PTFE depending on the cooling rate, X-ray diffraction (XRD) was employed. The XRD patterns show clear differences in crystallinity, showing amorphous, semi-crystalline, and crystalline PTFE (A-PTFE, SC-PTFE, and C-PTFE) (**Figure 1c**). A-PTFE and SC-PTFE show diffraction peaks, corresponding to (100), (110), (200), (108), (210), and (300) planes with a hexagonal structure, but have an amorphous region in the overall XRD patterns. The slight differences in the peak position of A-PTFE are because of the heat treatment to modify PTFE leading to a change in the interplanar spacings as well as the anisotropic orientation of the molecular chains of A-PTFE.[20] In contrast, the C-PTFE shows markedly sharp diffraction patterns with a strong intensity peak at 18° corresponding to the (100) plane and weak intensity peaks corresponding to (110), (200), (210), and (300) plans. The degree of crystallinity was determined based on the areas of crystalline peaks and the total area of crystalline and amorphous peaks.[21] The degree of crystallinity was 18.8, 41.3, and 88.1 % for A-PTFE, SC-PTFE, and C-PTFE, respectively. These results substantiate that the degree of crystallinity of PTFE can be varied by controlling the cooling rate, and PTFE has a high crystallinity when cooled at a slow cooling rate. In the Fourier transform infrared spectroscopy (FTIR) study, all the PTFE samples show apparent peaks at 1204.8 and 1148.8 cm^{-1} corresponding to the symmetric and asymmetric F-C-F stretching and at 637.4 cm^{-1} corresponding to the C-C stretching vibrations, which is considered to be insensitive to the crystallinity of PTFE (**Figure S1**).[22]

To evaluate the mechanical properties of PTFE depending on the crystallinity, a universal testing machine (UTM) was employed. **Figure 1d** shows the stress-strain curves of PTFE. As the degree of crystallinity of PTFE increases, the stress increases, and the strain is reduced, which means that the mechanical properties of PTFE have changed rigidly. In conventional LIBs, liquid electrolytes easily permeate into electrodes and facilitate charge transfer.[23] However, charger transfer has to occur at the interface between the physically adjacent particles in ASSBs.[24] Therefore, even a small volume change in CAMs can result in a loss of contact between particles, leading to a degradation of the electrochemical properties of cathodes (**Figure 1e**).[25] The increased mechanical properties of PTFE with higher crystallinity can mitigate the contact loss of particles in the cathode during cycling and can enable improved electrochemical performance.

To understand the electrochemical properties of cathodes with varying degrees of crystallinity of PTFE, NMC | LPSCl | Li cells were assembled. The synthesized LPSCl showed a high Li^{+} conductivity of 1.5 mS cm^{-1} (**Figure S2**).[2a] The AP-NMC cathodes were simply prepared by mixing the raw particles with a mortar and pestle. Due to the high electronegativity of the fluorine atoms, negative polarization (δ^-) is generated around PTFE, which prevents the aggregation between PTFE molecules, and thus easily forms micro-fibrilization by shear stress.[26] SCP-NMC and CP-NMC cathodes were prepared in the same manner with a different cooling rate after heating at 200 °C for 10 min. PTFE has a glass transition temperature of 127°C and a high melting point of 327 °C but begins to deteriorate at 260 °C.[27] Therefore 200 °C is selected as an optimum heating temperature.[28] All cathodes are freestanding flexible sheets, as shown in **Figure S3**. The XRD patterns of NMC cathodes show no clear difference, but the intensity of the peak at ~ 18° corresponding to the (100) plane of PTFE and (003) plane of NMC slightly increases as the degree of crystallinity of PTFE increases (**Figure S4**).[29] After heating only NMC, there is no change in the XRD peaks (**Figure S5**). The areal mass loading of NMC was 20 mg cm^{-2} (~4 mAh cm^{-2}) for all the NMC cathodes.

Figure 2a shows the initial voltage profiles of NMC cathodes at 0.05C rate. AP-NMC shows an initial discharge capacity of 171.0 mAh g^{-1} and a Coulombic efficiency (CE) of 69.1%. This low CE is understandable since bare Li and coating-free NMC were employed in this study. Compared to this, SCP-NMC and CP-NMC present improved capacities and CEs of, respectively, 175.0 mAh g^{-1} and 74.5 %, and 185.0 mAh g^{-1} and 76.4 %. There was no significant difference in the voltage profiles of cathodes prepared with pristine NMC and NMC after heat treatment (**Figure S6**). In addition, $LiNbO_3$-coated AP-NMC showed an improved discharging capacity of 177 mAh g^{-1} and a CE of 75.8% (**Figure S7**). The increase in the CEs of SCP-NMC and CP-NMC is not simply due to the different crystallinity of PTFE in NMC cathodes. At the initial charging, the decomposition of LPSCl is significantly lowered for SCP-NMC and CP-NMC. With the heat treatment applied to SCP-NMC and CP-NMC, LPSCl may be decomposed, and the CEI layer is preformed before cycling.[30] As a result, the decomposition slope at the initial charging is reduced (**Figure 2a** inset).[31] Furthermore, the electronic conductivity of NMC cathodes measured by DC polarization was lowered in the order of AP-NMC > SCP-NMC > CP-NMC, with the corresponding values of, respectively, 6.7, 3.7, and 2.3 mS cm^{-1} (**Figure S8**). The electronically conductive surfaces of AP-NMC would accelerate the decomposition of LPSCl, resulting in poor CE. On the other hand, Li$^+$ conductivities of the cathodes showed no significant difference, showing 1.9, 2.0, and 2.1 $\times$ 10^{-4} S cm^{-1} for, respectively, AP-NMC, SCP-NMC, and CP-NMC (**Figure S9**).[32]

Figure 2b shows the rate capability of NMC cathodes up to 1C rate. CP-NMC and SCP-NMC exhibited a higher discharge capacities of 129 and 118 mAh g^{-1} compared to AP-NMC (107 mAh g^{-1}) at 1C rate. After that, all the NMC cathodes retained the orgninal discharge capacities at 0.1C rate. Discharge voltage profiles observed by galvanostatic intermittent titration technique (GITT) and the corresponding polarization curves are displayed in **Figure 2c,d**. The lowered polarization for CP-NMC and SCP-NMC is verified at a current density of 0.8 mA cm^{-2} (0.2C rate) in the whole range. At a low current density of 0.2 mA cm^{-2} (0.05 C), there was no significant difference in polarization for NMC cathodes (**Figure S10**). The cycle performances of NMC cathodes with varying degrees of PTFE crystallinity show a stark contrast at 0.1C rate for 200 cycles (**Figure 2e**). AP-NMC shows fast capacity fading at earlier cycles and a capacity retention of 64.1 % from 2 to 200 cycles. SCP-NMC shows a slowly decreasing capacity, but there was no big difference in the retention of 69.6 % at 200 cycles compared to that of AP-NMC. On the other hand, CP-NMC exhibits an outstanding capacity retention of 84.1 % at 200 cycles. Furthermore, SCP-NMC and CP-NMC showed improved initial discharging capacities and CEs of, respectively, 193 mAh g^{-1} and 83.6 %, and 202 mAh g^{-1} and 87.6 % at 60 °C (Figure S11). Those improvements can be explained to be due to the improved interfacial stability between the CAMs and SEs provided by the initially formed CEI layer during heat treatment at 200 °C.[30] The improved cycle and rate performances of CP-NMC can be explained in two aspects. First, the rigid mechanical property of C-PTFE enables the maintenance of intimate contacts between particles in the cathode, facilitating a homogeneous charge transfer. Second, the preformed CEI layer suppresses the decomposition of LPSCl with CAMs.

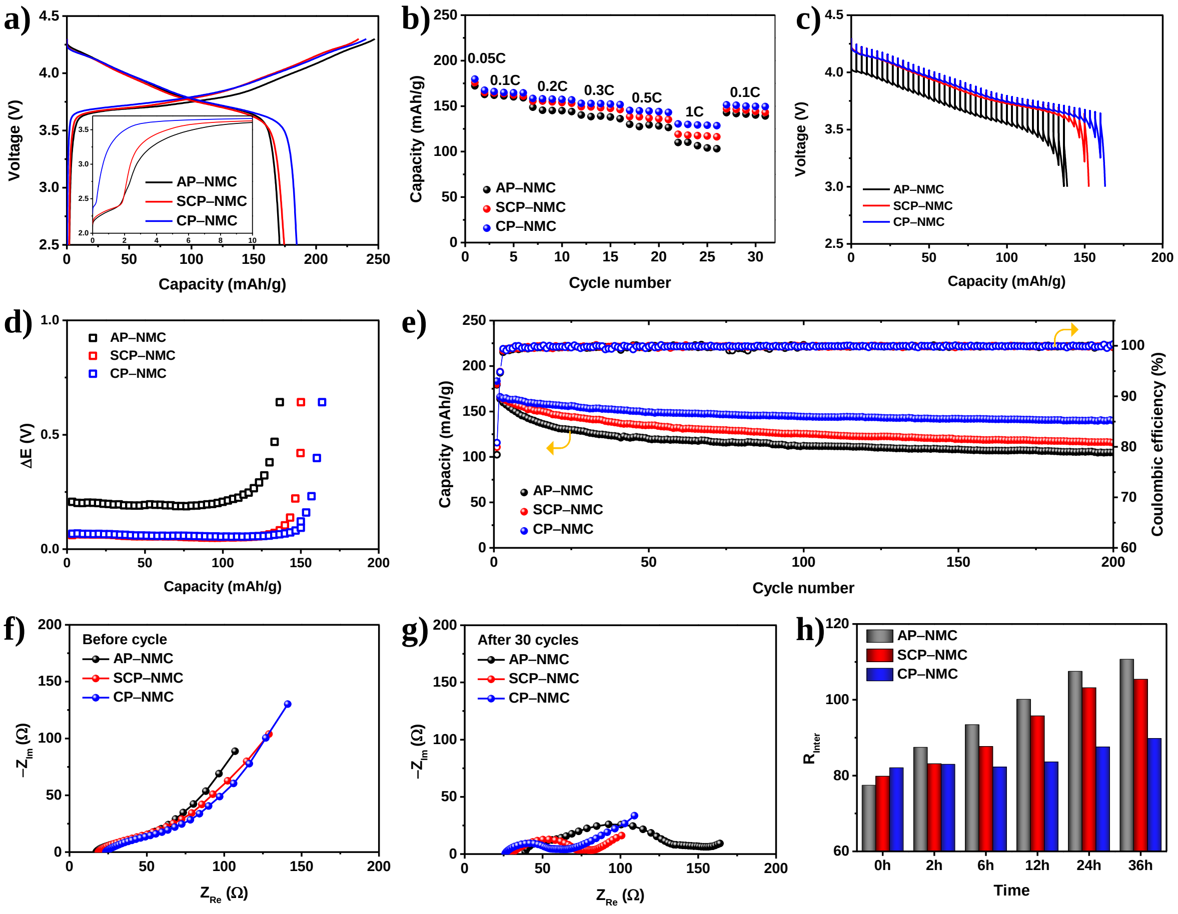

Figure 2. Electrochemical performances of the NMC | LPSCl | Li cells. (a) Initial voltage profiles. (b) Rate capability at various rates from 0.1C to 1C. (c) Voltage profiles and (d) corresponding polarization plots obtained with GITT at 0.2C rate. e) Cycle performance at 0.1C rate at room temperature. Nyquist plots (f) before cycling and (g) after 30 cycles. (h) Interfacial resistances (R_{Inter}) of cathodes with resting time at the initial charged state.

EIS studies were carried out to understand the interfacial resistances of NMC cathodes. The pristine SCP-NMC and CP-NMC before cycling showed slightly higher interfacial resistances (R_{Inter}) of 31.3 and 32.3 Ω compared to that of AP-NMC (25.7 Ω) (**Figure 2f**). It can be inferred that the CEI layer is generated by the decomposition of LPSCl due to the chemical incompatibility between NMC and LPSCl, and this effect is intensified during the heat treatment process.[33] However, CP-NMC showed a lower R_{Inter} of 35.1 Ω compared to that of SCP-NMC (39.4 Ω) and AP-NMC (59.0 Ω) after 30 cycles. Generally, severe degradation is triggered by an incompatibility between NMC and LPSCl at a high state of charge.[34] In this study, the EIS of NMC cathodes with resting time was measured at a fully charged state. The evolution of R_{Inter} of NMC cathodes upon resting at the initially charged state shows clear differences (**Figure 2h and S12**). However, there was no difference in the evolution of R_{Inter} after resting at the discharged state (**Figure S13**). The continuous formation of the CEI layer with prolonged cycling in sulfide-based ASSBs is usually the key reason for the capacity fade.[35] In the case of CP-NMC, further formation of CEI was not significant due to the improved robustness of the cathode.

To gain insight into the nature of the CEI layer, XPS measurements were carried out before and after cycling (**Figure 3a-f**). The S 2p spectrum of LPSCl consists of a main doublet for the S $2p_{3/2}$ at a binding energy of 161.7 eV (orange component), which corresponds to the PS_4^{3-} units of LPSCl. A weak doublet at a binding energy of 160.5 eV (blue component) can be attributed to the remaining Li_2S after the synthesis of LPSCl. The third minor doublet at a binding energy of 162.8 eV (cyan component) corresponds to P_2S_5 and is probably related to the oxidized sulfur species ($P_2S_6^{-2}$).[36] A doublet peak at a higher binding energy of 163.5 eV (purple component) is also attributed to LPSCl-derived bridging sulfur species (P-S-P groups). All pristine NMC cathodes showed a similar trend in the formation of oxidized sulfur species, which means that the NMC-LPSCl interface is unstable. However, SCP-NMC and CP-NMC exhibited higher intensity at a binding energy of 162.8 and 163.5 eV compared to AP-NMC.

This can be inferred that the CEI layer with oxidized species derived from LPSCl was intensified, and accordingly, the interfacial resistance increased and the electronic conductivity decreased for SCP-NMC and CP-NMC.

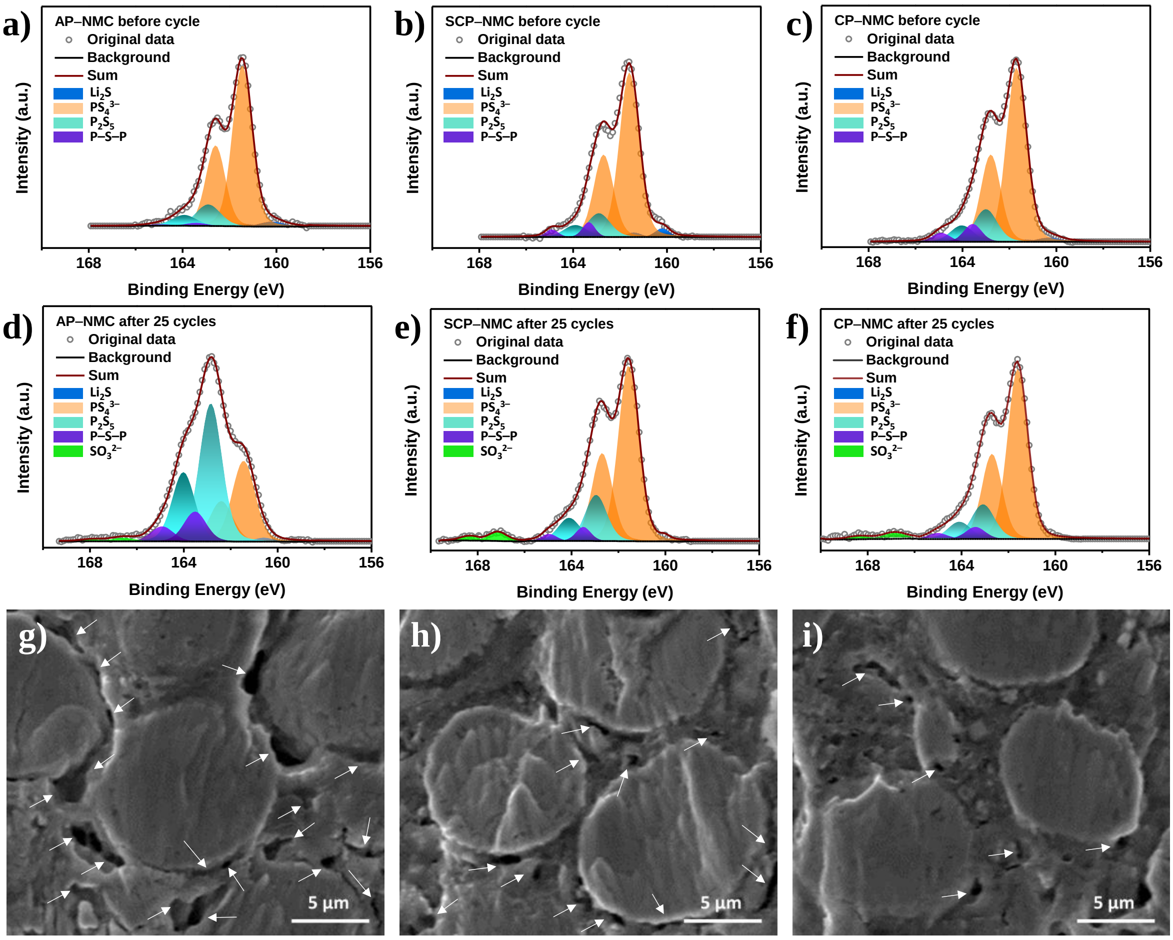

Figure 3. XPS spectra of the S 2p core-level regions of the cathodes (a-c) before cycling and (d-f) after 25 cycles at 0.1C rate at room temperature. Cross-sectional SEM images of (g) AP-NMC, (h) SCP-NMC, and (i) CP-NMC after 25 cycles.

To further investigate the CEI layer after cycling, cycled NMC cathodes were investigated by XPS (**Figure 3d-f**). AP-NMC exhibits clearly different S 2p spectra after cycling. A new doublet at a binding energy of 167.1 eV was generated, corresponding to sulfite (SO_3^{2-}) at the surface.[7] The intensity of the main doublet at a binding energy of 161.7 eV was noticeably decreased and the doublet peaks at a binding energy of 162.8 and 163.5 eV were significantly increased. These changes of S 2p signals of AP-NMC substantiate that a significant interface reaction between NMC and LPSCl occurred during cycling. SCP-NMC also showed increased doublet peaks at a binding energy of 162.8 and 163.5 eV and a new doublet at a binding energy of 167.1. Considering the overall S 2p signals, SCP-NMC exhibited fewer interfacial resistive layers compared to AP-NMC. Contrary to AP-NMC and SCP-NMC, CP-NMC exhibited a negligible increase in the intensities of the doublet peaks at a binding energy of 162.8 and 163.5 eV. Generally, active materials with volume changes associated with Li^+ insertion/desertion have issues related to the cumulative interfacial resistive layer because of the newly formed interfaces during cycling.[37] LPSCl has a narrow electrochemical stability window of 1.7 – 2.3 V vs. Li/Li^+, so even small volume changes of CAMs can generate localized high current density with inhomogeneous contact between particles and accelerate a cumulative formation of the CEI layer.[38] Therefore, the crystalline PTFE can act as a robust binder to mitigate the volumetric stress and accordingly reduce the continuous formation of the CEI layer during cycling.

The cross-sectional SEM images were obtained to clarify the contact loss in NMC cathodes after cycles, as shown in **Figure 3g-I and S14**. The SEM images exhibit a clear difference in particle contact after 25 cycles. AP-NMC shows many void spaces, which induce electrochemical isolation of CAMs, resulting in poor electrochemical properties in ASSBs. Furthermore, the presence of void spaces proves that new interfaces between NMC and LPSCl can be formed due to the volume changes of CAMs, and CEI layers can be accumulated. Accordingly, the deteriorating interfaces upon cycling result in a heterogeneous electrochemical reaction and accelerated fast capacity fade.[39] Compared to this, SCP-NMC and CP-NMC show fewer void spaces with intimate contacts between particles due to the improved mechanical robustness induced by the crystallinity of PTFE. The degree of crystallinity of PTFE plays a role in the improved electrochemical properties in ASSBs by mechanically reinforcing the cathodes.

3. Conclusions

In this work, we revealed that the physicochemical properties of PTFE have a significant effect on the electrochemical performance of cathodes in ASSBs. Solvent-free NMC cathodes with PTFE as a binder with different crystallinity were prepared by controlling the cooling rate after heating. As the degree of crystallinity of PTFE increased, NMC cathodes showed improved electrochemical properties. Especially, the CP-NMC cathode exhibited outstanding cycle performance with the retention of 84.1 % at 200 cycles and high rate capabilities up to 1C rate. Furthermore, the CEI layers were initially generated due to the chemical incompatibility between NMC and LPSCl. With EIS measurement, it was verified that those CEI layers induced lower electronic conductivity and higher R_{Inter}. However, cathodes with high crystalline PTFE showed lower and stable R_{Inter} at the initially charged state and after cycles. Through postmortem SEM and XPS studies, it was found that interfacial resistive layers were not significantly generated during cycling due to the intimate contacts of mechanically reinforced cathodes with high crystalline PTFE. This simple, but effective, strategy can provide insight into the design of cathodes and utilize solvent-free PTFE-based cathodes with a variety of CAMs and SEs for ASSBs.

4. Experimental Section

4.1 Preparation of materials

To characterize PTFE, the PTFE films were prepared by rolling PTFE (Sigma Aldrich) powders. To control the degree of crystallinity of PTFE, the PTFE films were heated up to

200 °C at a heating rate of 5 °C min^{-1} and cooled down to room temperature as a function of cooling rate (15 °C min^{-1} for semi-crystalline PTFE (SC-PTFE) and 2 °C min^{-1} for crystalline PTFE (C-PTFE)). LPSCl, with a conductivity of > 1 mS cm^{-1} at room temperature, was synthesized by mechanochemical process. Precisely, a stoichiometric mixture of LiCl (99.9% Sigma Aldrich), Li_2S (99.9% Sigma Aldrich) and P_2S_5 (99.99% Sigma Aldrich) was ball milled at 500 rpm for 20 h in a ZrO_2 milling jar with ZrO_2 milling balls, followed by additional heat treatment at 600 °C for 5 h at an Ar atmosphere. To obtain the uniform size distribution of LPSCl, the as prepared powder was ball milled at 500 rpm for 3 h in the same manner. $Ni_{0.8}Mn_{0.1}Co_{0.1}(OH)_2$ presurcor was synthesized via a hydroxide coprevipitation method as reported previously.[29] Precisely, 1 M aqueous salt solution ($NiSO_4 \cdot 6H_2O$, $MnSO_4 \cdot H_2O$, $CoSO_4 \cdot 7H_2O$), 2 M KOH in water, and 5 M NH_4OH were concurrently pumped into the tank reactor at 50 °C and pH≈10 – 11 with stirring at 700 rpm. After feeding the solution, the obtained precursor was washed with deionized water and collected after filtering. After that, the precursor was dried overnight at 110 °C. Finally, $LiNi_{0.8}Mn_{0.1}Co_{0.1}O_2$ (NMC811) was obtained by calcining the dried precursor with LiOH with a Li to transition metal molar ratio of 1.03 at 770 °C for 15 h under O_2 atmosphere. $LiNbO_3$ (1 wt%) was coated on NMC811 by a wet-chemical method using lithium ethoxide and niobium ethoxide in ethanol. To prepare the solvent-free PTFE-based cathodes, NMC, LPSCl, carbon nanofiber (CNF, Sigma Aldrich), and PTFE were mixed with a mortar and pestle in a weight ratio of 70 : 27 : 2 : 1 and rolled with a stainless-steel rod. To control the degree of crystallinity of PTFE in the cathodes, the prepared cathodes were heated and cooled as explained above.

4.2 Material characterization

To analyze the crystallinity of PTFE, powder X-ray diffraction (XRD, Rigaku Miniflex 600) measurements were carried out at room temperature employing Cu K_α radiation in the rage of 10 – 60° (1° min^{-1}). The degree of crystallinity of PTFE was calculated by the equation $\frac{A_c}{A_c+A_a}\times 100$, where A_c is the area of crystalline peaks and A_a is the area of amorphous region. Fourier-transform infrared spectra (FTIR) of PTFE were collected with a Thermofisher FTIR Spectrometer. The mechanical properties of PTFE were obtained with a universal testing machine (UTM, TA instruments). To characterize the surface of NMC cathodes before and after cycling, X-ray photoelectron spectrometry (Kratos XPS) was employed. The binding energy was calibrated with the reference C 1s peak as 284.5 eV and the spectra were analyzed with CasaXPS software. To investigate particle contacts in cathodes after cycling, cross-sectional SEM images were obtained with a scanning electron microscopy (SEM, FEI Quanta 650). The cross-sectional electrodes were prepared by Ar ion milling (Hitachi Ion Mill).

4.3 Electrochemical characterization

The electrochemical characterization was conducted with custom-made stainless-steel cells. To assemble ASSBs, the freestanding NMC cathode was placed into a polyether ether ketone (PEEK) cylinder (12.7 mm diameter) and pressed at 400 MPa for 1 min, and then ~150 mg of LPSCl power was spread over the NMC cathode pellet and pressed at 385 MPa. Finally, Li metal foil was attached to the LPSCl side. The prepared cells were evaluated at the voltage window of 4.3 – 2.5 V with a constant pressure of 50 MPa during cycling. All cycling tests were conducted with an Arbin cycler. The galvanostatic intermittent titration technique (GITT) measurements were conducted with a pulse current of 0.8 mA cm^{-2} (0.2 C) and rest for 2 h. The electrochemical impedance spectroscopy (EIS) data were collected with an amplitude of 10 mV in the frequency range od 1 MHz to 10 mHz with a potentiostat (BioLogic). To measure the electronic conductivity of NMC cathodes, ionic blocking cells (SUS | NMC | SUS) were assembled. In detail, freestanding NMC cathode was placed into a PEEK cylinder and pressed at 400 MPa for 1 min with stainless steel rods. The constant voltage of 500 mV was applied to the ionic blocking cells for 10 min.

Supporting Information

Supporting Information is available from the Wiley Online Library or from the author.

Acknowledgments

This work was supported by the Assistant Secretary for Energy Efficiency and Renewable Energy, Office of Vehicle Technologies of the U.S. Department of Energy through the Advanced Battery Materials Research (BMR) Program (Battery500 Consortium) award number DE-EE0007762.

References

[1] S. Randau, D. A. Weber, O. Kötz, R. Koerver, P. Braun, A. Weber, E. Ivers-Tiffée, T. Adermann, J. Kulisch, W. G. Zeier, Nature Energy 2020, 5, 259.

[2] a) Y. Kato, S. Hori, T. Saito, K. Suzuki, M. Hirayama, A. Mitsui, M. Yonemura, H. Iba, R. Kanno, Nature Energy 2016, 1, 1; b) L. Zhou, A. Assoud, Q. Zhang, X. Wu, L. F. Nazar, Journal of the American Chemical Society 2019, 141, 19002; c) N. Kamaya, K. Homma, Y. Yamakawa, M. Hirayama, R. Kanno, M. Yonemura, T. Kamiyama, Y. Kato, S. Hama, K. Kawamoto, Nature materials 2011, 10, 682.

[3] M. Weiss, F. J. Simon, M. R. Busche, T. Nakamura, D. Schröder, F. H. Richter, J. Janek, Electrochemical Energy Reviews 2020, 3, 221.

[4] A. Banerjee, X. Wang, C. Fang, E. A. Wu, Y. S. Meng, Chemical reviews 2020, 120, 6878.

[5] a) Y. Li, Y. Wu, T. Ma, Z. Wang, Q. Gao, J. Xu, L. Chen, H. Li, F. Wu, Advanced Energy Materials 2022, 12, 2201732; b) F. Hippauf, B. Schumm, S. Doerfler, H. Althues, S. Fujiki, T. Shiratsuchi, T. Tsujimura, Y. Aihara, S. Kaskel, Energy Storage Materials 2019, 21, 390.

[6] J. Lau, R. H. DeBlock, D. M. Butts, D. S. Ashby, C. S. Choi, B. S. Dunn, Advanced Energy Materials 2018, 8, 1800933.

[7] J. Auvergniot, A. Cassel, D. Foix, V. Viallet, V. Seznec, R. Dedryvère, Solid State Ionics 2017, 300, 78.

[8] a) L. Peng, H. Ren, J. Zhang, S. Chen, C. Yu, X. Miao, Z. Zhang, Z. He, M. Yu, L. Zhang, Energy Storage Materials 2021, 43, 53; b) Y. Xiao, Y. Wang, S.-H. Bo, J. C. Kim, L. J. Miara, G. Ceder, Nature Reviews Materials 2020, 5, 105; c) J. H. Woo, J. J. Travis, S. M. George, S.-H. Lee, Journal of The Electrochemical Society 2014, 162, A344.

[9] S. S. Zhang, Energy Storage Materials 2020, 24, 247.

[10] J. Ruhl, L. M. Riegger, M. Ghidiu, W. G. Zeier, Advanced Energy and Sustainability Research 2021, 2, 2000077.

[11] E. Dhanumalayan, G. M. Joshi, Advanced Composites and Hybrid Materials 2018, 1, 247.

[12] T. Kitahara, K. Hosokawa, T. Shimizu, Google Patents, 2003.

[13] C. Wang, R. Yu, H. Duan, Q. Lu, Q. Li, K. R. Adair, D. Bao, Y. Liu, R. Yang, J. Wang, ACS Energy Letters 2021, 7, 410.

[14] G. J. Puts, P. Crouse, B. M. Ameduri, Chemical reviews 2019, 119, 1763.

[15] B. Ameduri, Chemical reviews 2009, 109, 6632.

[16] a) R. Eby, E. Clark, B. Farmer, G. Piermarini, S. Block, Polymer 1990, 31, 2227; b) E. Clark, Polymer 1999, 40, 4659.

[17] E. Brown, P. Rae, D. Dattelbaum, B. Clausen, D. Brown, Experimental mechanics 2008, 48, 119.

[18] E. N. Brown, D. M. Dattelbaum, Polymer 2005, 46, 3056.

[19] A. Galeski, Progress in Polymer Science 2003, 28, 1643.

[20] A. S. Smolyanskii, E. D. Politova, O. g. A. Koshkina, M. A. Arsentyev, P. P. e. Kusch, L. V. Moskvitin, S. V. e. Slesarenko, D. P. Kiryukhin, L. I. Trakhtenberg, Polymers 2021, 13, 3678.

[21] N. Murthy, H. Minor, Polymer 1990, 31, 996.

[22] H. W. Starkweather Jr, R. C. Ferguson, D. B. Chase, J. M. Minor, Macromolecules 1985, 18, 1684.

[23] D. Lee, H. Lee, T. Song, U. Paik, Advanced Energy Materials 2022, 2200948.

[24] R. Chen, Q. Li, X. Yu, L. Chen, H. Li, Chemical reviews 2019, 120, 6820.

[25] J. Ma, B. Chen, L. Wang, G. Cui, Journal of Power Sources 2018, 392, 94.

[26] Y. Li, Y. Wu, Z. Wang, J. Xu, T. Ma, L. Chen, H. Li, F. Wu, Materials Today 2022.

[27] P. Rae, D. Dattelbaum, Polymer 2004, 45, 7615.

[28] D. Hirai, E. Climent-Pascual, R. J. Cava, Physical Review B 2011, 84, 174519.

[29] Q. Xie, Z. Cui, A. Manthiram, Advanced Materials 2021, 33, 2100804.

[30] T.-T. Zuo, F. Walther, S. Ahmed, R. Rueß, J. Hertle, B. Mogwitz, K. Volz, J. r. Janek, ACS Energy Letters 2023, 8, 1322.

[31] D. H. Tan, Y.-T. Chen, H. Yang, W. Bao, B. Sreenarayanan, J.-M. Doux, W. Li, B. Lu, S.-Y. Ham, B. Sayahpour, Science 2021, 373, 1494.

[32] D. Y. Oh, Y. J. Nam, K. H. Park, S. H. Jung, K. T. Kim, A. R. Ha, Y. S. Jung, Advanced Energy Materials 2019, 9, 1802927.

[33] J. Jang, Y.-T. Chen, G. Deysher, D. Cheng, S.-Y. Ham, A. Cronk, P. Ridley, H. Yang, B. Sayahpour, B. Han, ACS Energy Letters 2022, 7, 2531.

[34] T.-T. Zuo, R. Rueß, R. Pan, F. Walther, M. Rohnke, S. Hori, R. Kanno, D. Schröder, J. Janek, Nature communications 2021, 12, 1.

[35] R. Koerver, F. Walther, I. Aygün, J. Sann, C. Dietrich, W. G. Zeier, J. Janek, Journal of Materials Chemistry A 2017, 5, 22750.

[36] Y. Han, S. H. Jung, H. Kwak, S. Jun, H. H. Kwak, J. H. Lee, S. T. Hong, Y. S. Jung, Advanced Energy Materials 2021, 11, 2100126.

[37] H. Wu, G. Chan, J. W. Choi, I. Ryu, Y. Yao, M. T. McDowell, S. W. Lee, A. Jackson, Y. Yang, L. Hu, Nature nanotechnology 2012, 7, 310.

[38] D. H. Tan, E. A. Wu, H. Nguyen, Z. Chen, M. A. Marple, J.-M. Doux, X. Wang, H. Yang, A. Banerjee, Y. S. Meng, ACS Energy Letters 2019, 4, 2418.

[39] S. Lou, Q. Liu, F. Zhang, Q. Liu, Z. Yu, T. Mu, Y. Zhao, J. Borovilas, Y. Chen, M. Ge, Nature communications 2020, 11, 1.

Table of contents Entry

Sonvent-free cathodes with PTFE binders with different crystallinity are investigated, for the first time, in all-solid-state batteries (ASSBs). The work reveals that highly crystalline PTFE enables intimate contact and stable interfaces of the cathode by heat history, leading to significantly improved cycling performance in ASSBs.

Dongsoo Lee and Arumugam Manthiram*

Stable Cycling with Intimate Contacts Enabled by Crystallinity-controlled PTFE-based Solvent-free Cathodes in All-solid-state Batteries

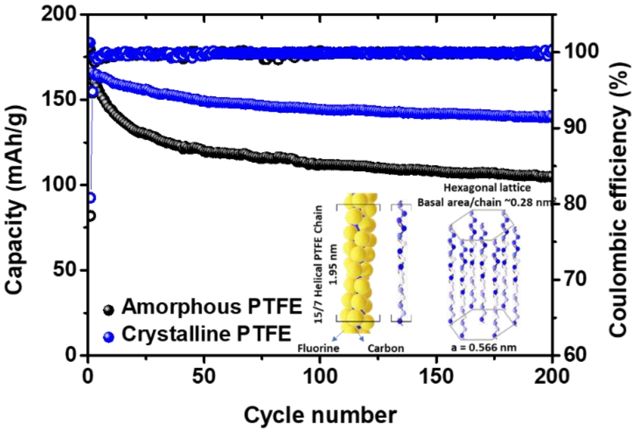

Supporting Information

Stable Cycling with Intimate Contacts Enabled by Crystallinity-controlled PTFE-based Solvent-free Cathodes in All-solid-state Batteries

Dongsoo Lee, and Arumugam Manthiram*

Materials Science and Engineering Program & Texas Materials Institute
The University of Texas at Austin, Austin, TX, 78712-1591 USA

*Corresponding Author
E-mail: rmanth@mail.utexas.edu

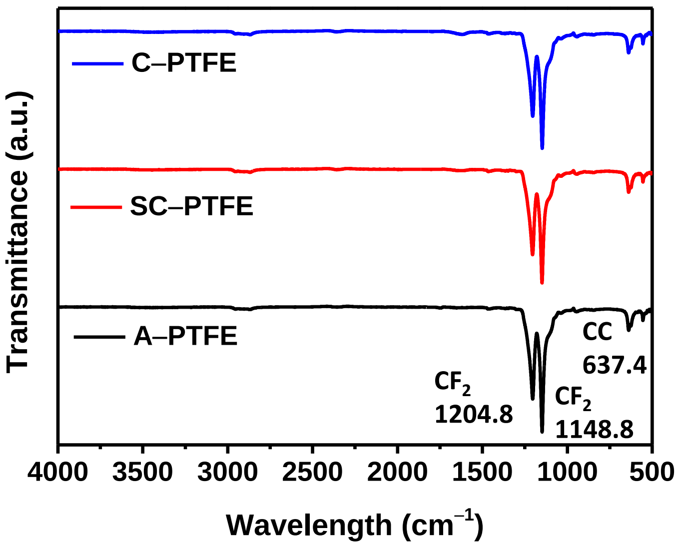

Figure S1. FT-IR spectra of P-PTFE, SC-PTFE, and C-PTFE.

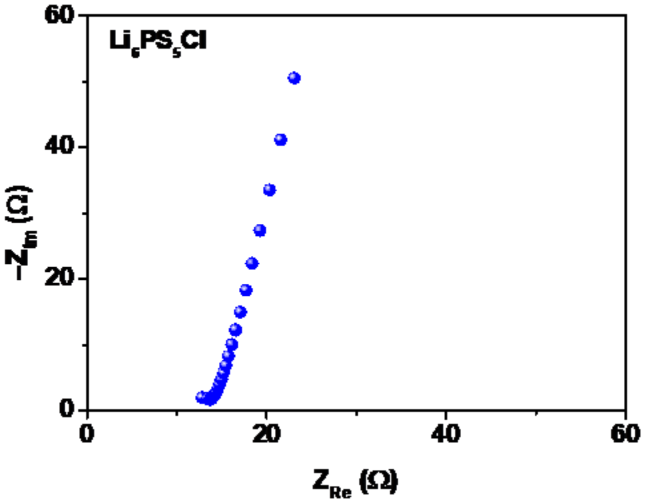

Figure S2. Nyquist plot of the synthesized Li_6PS_5Cl pellet to verify the Li^+ conductivity. To prepare the pellet, Li_6PS_5Cl powder was placed into a peek cylinder with stainless steel rod at both sides and pressed at 390 Mpa for 2 min. The thickness and diameter of the pellet were, respectively, 0.028 cm and 1.27 cm. EIS was performed with 10 mV constant voltage within a frequency range of 1 MHz to 100 mHz.

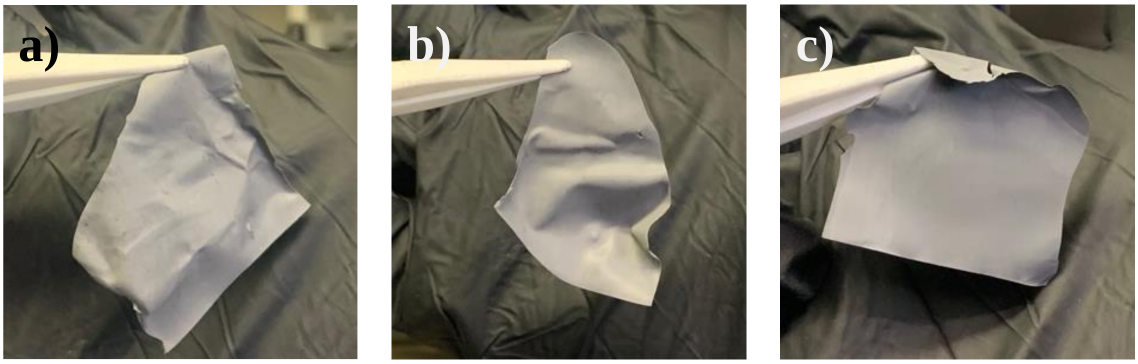

Figure S3. Digital photographs of AP–NMC, SCP–NMC, and CP–NMC.

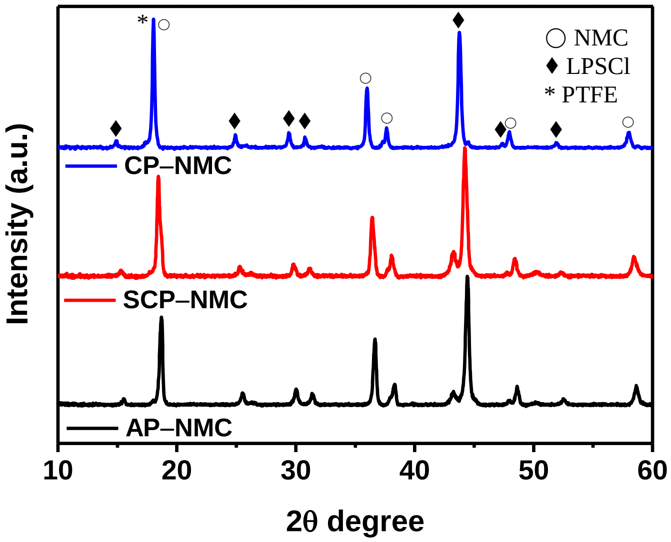

Figure S4. XRD patterns of AP-NMC, SCP-NMC, and CP-NMC before cycling.

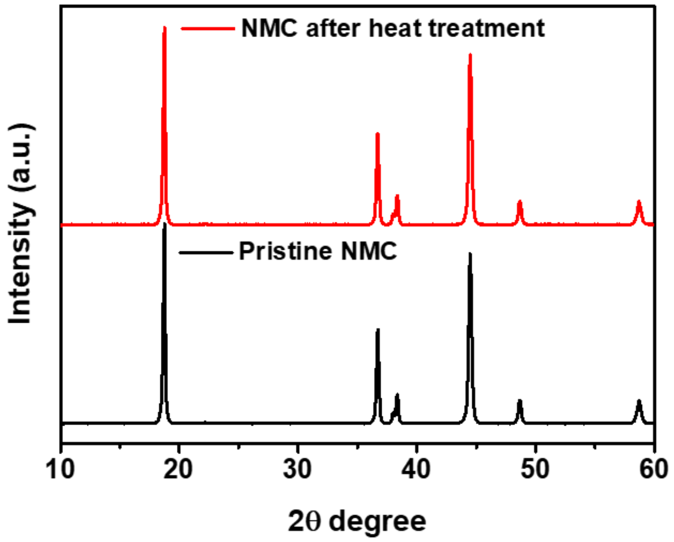

Figure S5. XRD patterns of the pristine NMC and NMC after heat treatment at 200 °C for 10 min under an Ar atmosphere (heating ratio of 5 °C min^{-1} and cooling ratio of 5 °C min^{-1}).

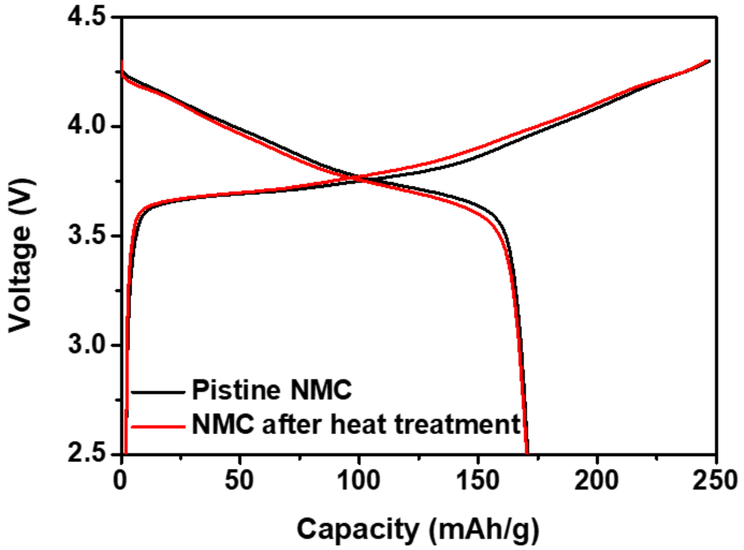

Figure S6. Initial voltage profiles of the cathodes prepared with the pristine NMC and NMC after heat treatment at 200 °C for 10 min (heating ratio of 5 °C min^{-1} and cooling ratio of 5 °C min^{-1}) under Ar atmosphere at room temperature.

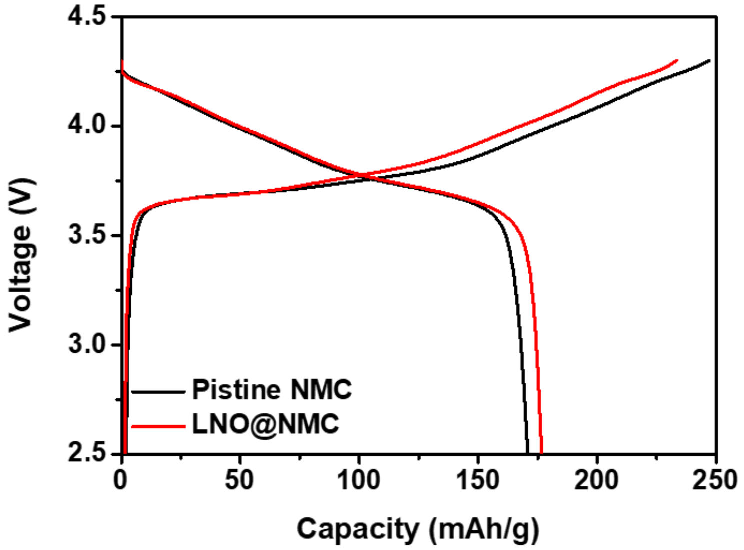

Figure S7. Initial voltage profiles of the cathodes prepared with the pristine NMC and $LiNbO_3$ coated NMC (LNO@NMC) at room temperature.

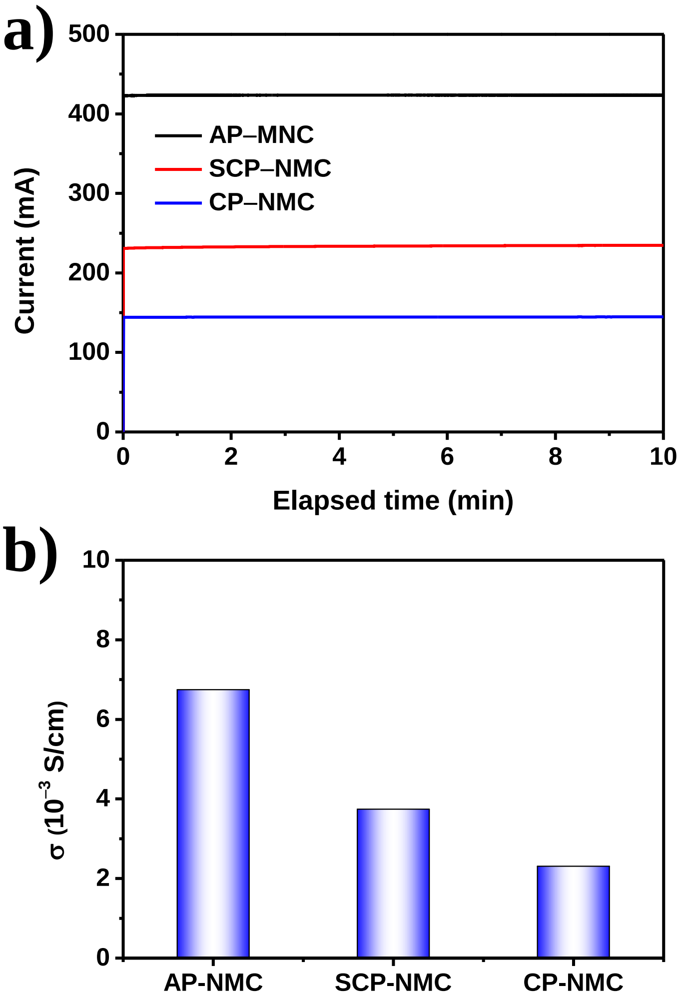

Figure S8. (a) Current vs. elapsed time of NMC cathodes by DC polarization method with ionic blocking cells SUS | NMC | SUS (SUS refers to stainless steel) with a constant voltage of 500 mV, and the corresponding (b) electronic conductivity of AP-NMC, SCP-NMC, and CP-NMC.

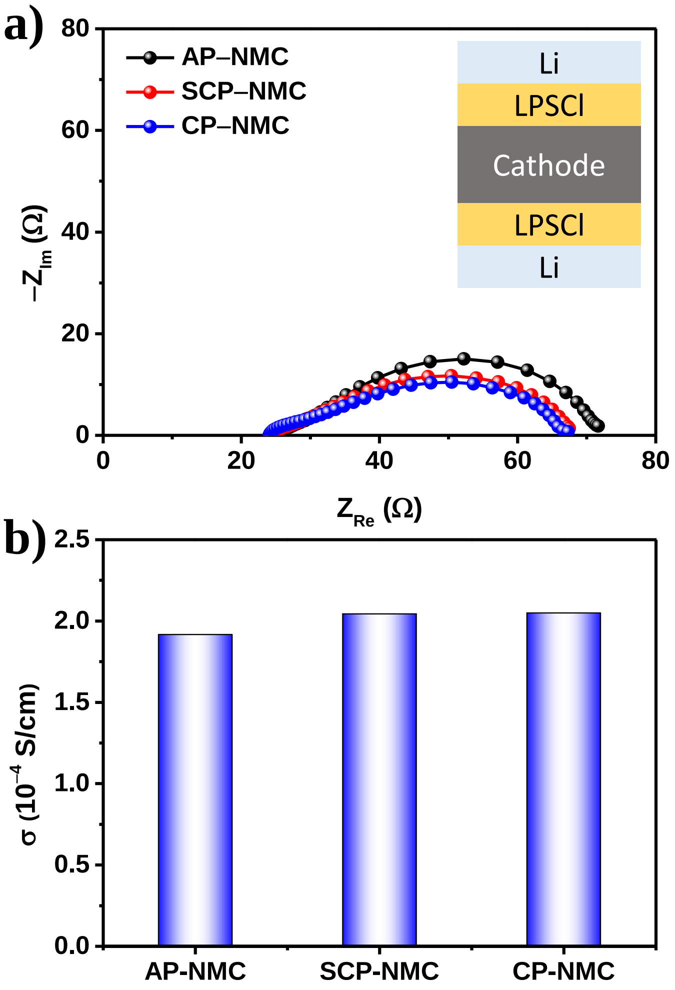

Figure S9. (a) Nyquist plots of AP–NMC, SCP–NMC, and CP–NMC. Electron-blocking Li/LPSCl/cathode/LPSCl/Li cells were employed to observe Li^+ conductivity of the cathodes. In the high frequency region, the x-axis intersection is assigned to Li^+ ionic resistance of LPSCl layers, and the overall semicircles are assigned to Li^+ ionic resistance of the cathode. (b) Li^+ conductivity of AP–NMC, SCP–NMC, and CP–NMC. EIS was performed with 10 mV constant voltage within a frequency range of 1 MHz to 100 mHz.

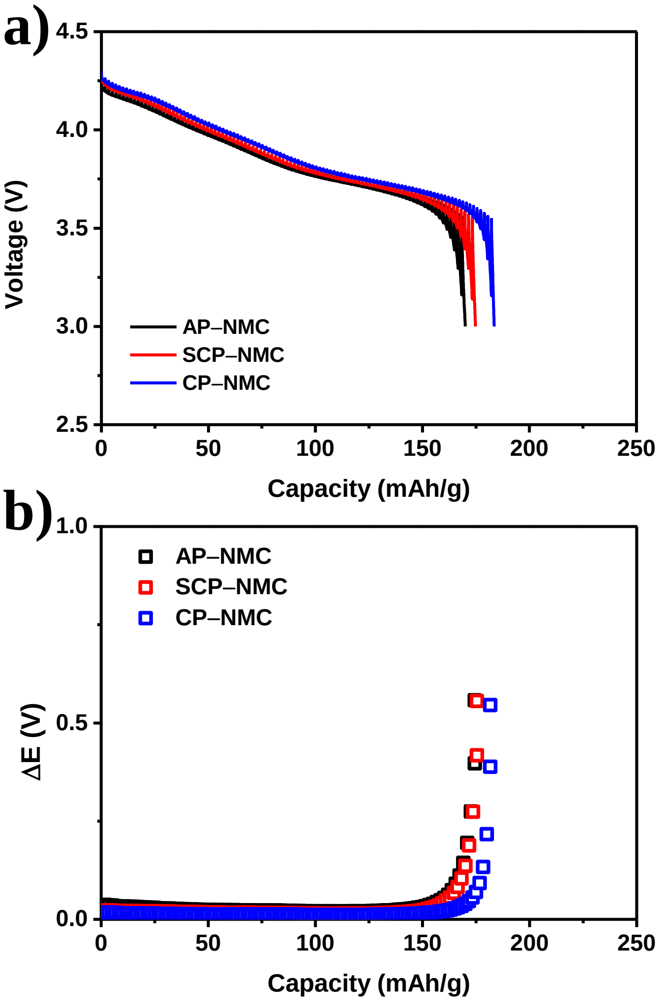

Figure S10. (a) Voltage profiles and (b) corresponding polarization plots obtained by GITT with a pulse current of 0.2 mA cm^{-2} (0.05 C) and rest for 10 min.

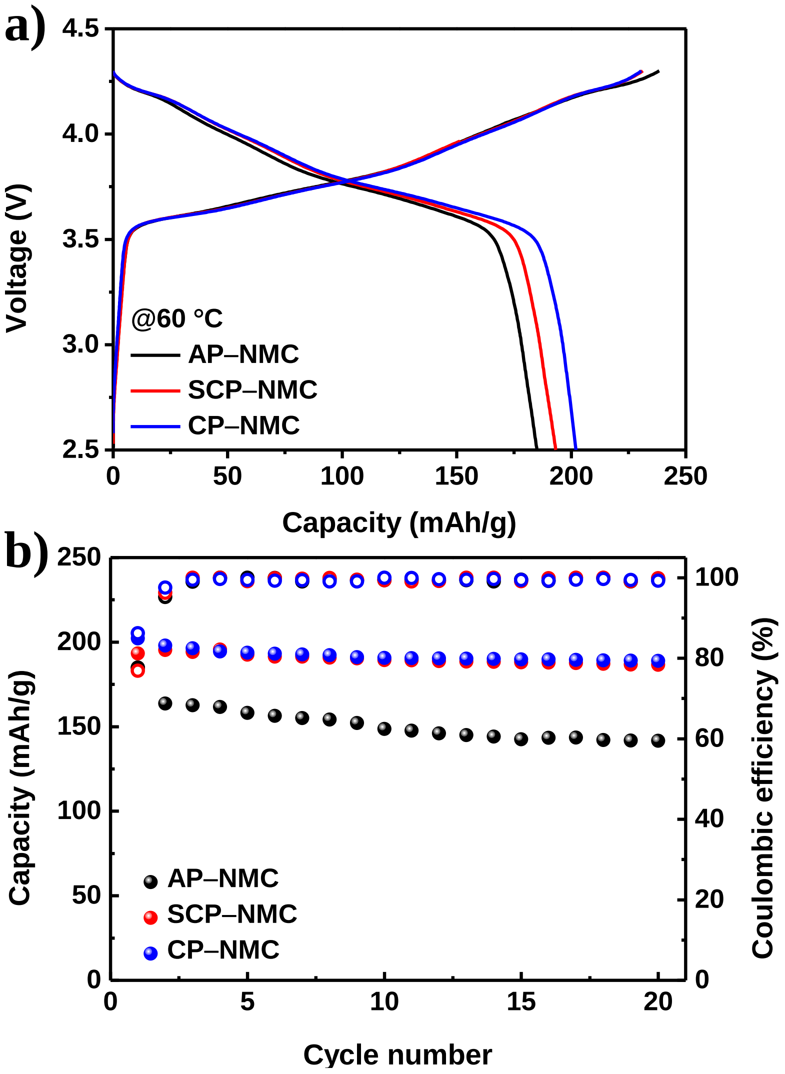

Figure S11. (a) Initial voltage profiles and (b) cycling performance of AP-NMC, SCP-NMC and CP-NMC at 60 °C.

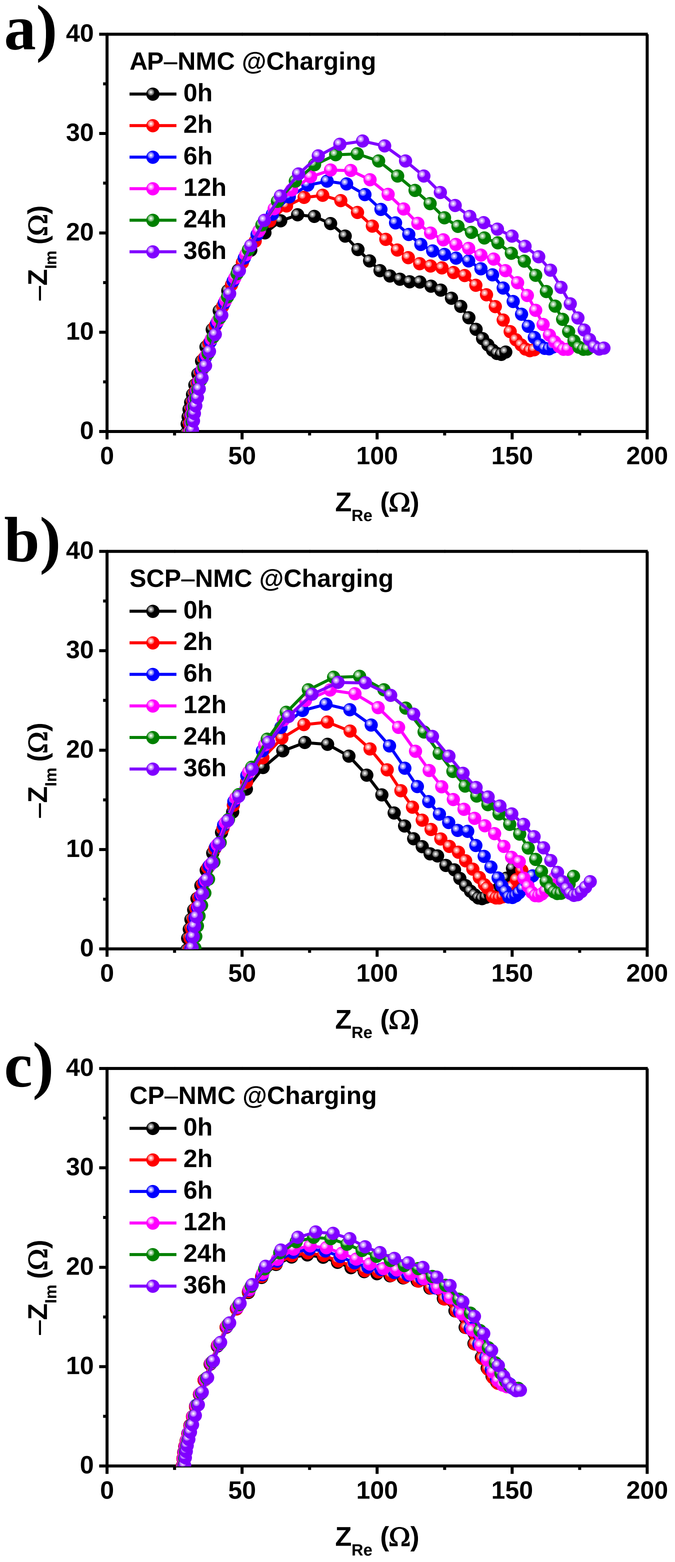

Figure S12. Nyquist plots of (a) AP-NMC, (b) SCP-NMC, and (c) CP-NMC over time at the initially charged state at 0.05C rate. EIS was performed with 10 mV constant voltage within a frequency range of 1 MHz to 100 mHz.

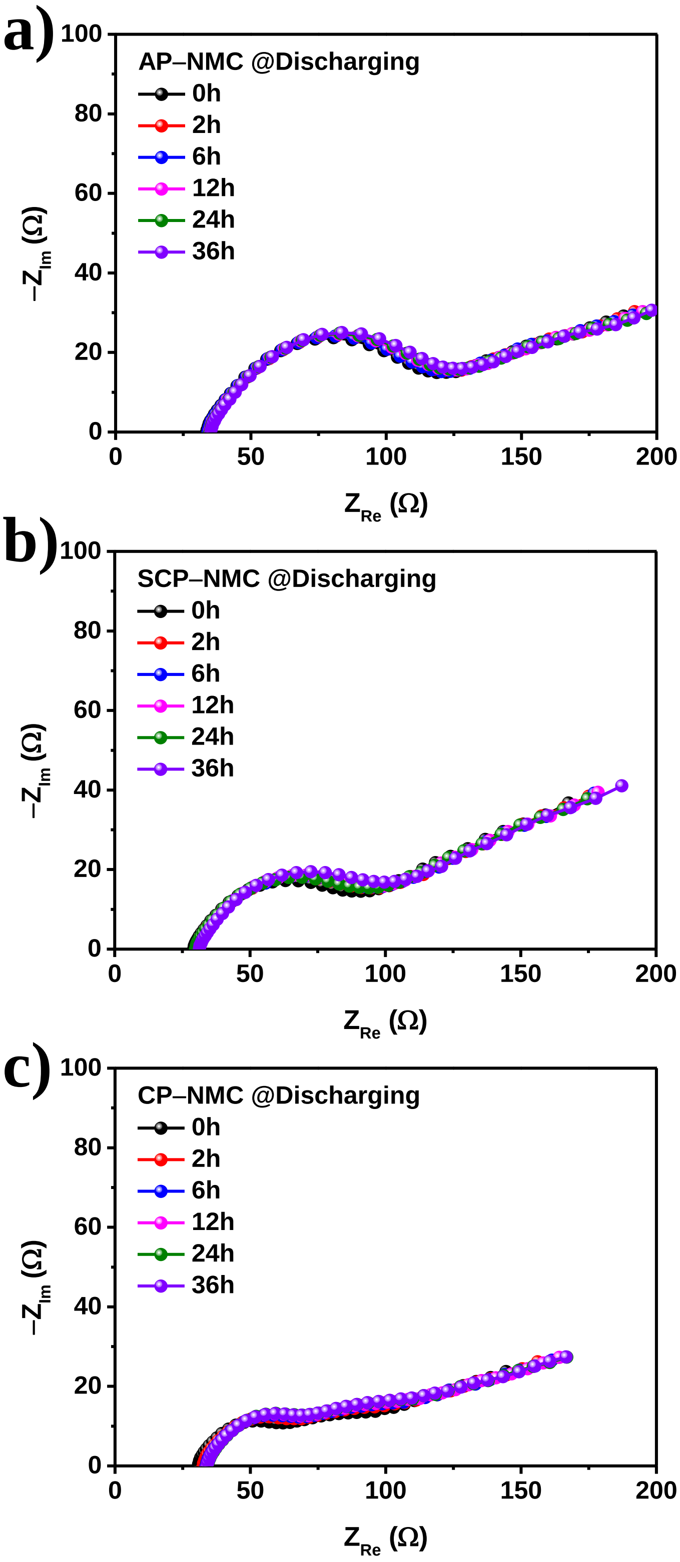

Figure S13. Nyquist plots of (a) AP-NMC, (b) SCP-NMC, and (c) CP-NMC over time at the initially discharged state after charging at 0.05C rate. EIS was performed with 10 mV constant voltage within a frequency range of 1 MHz to 100 mHz.

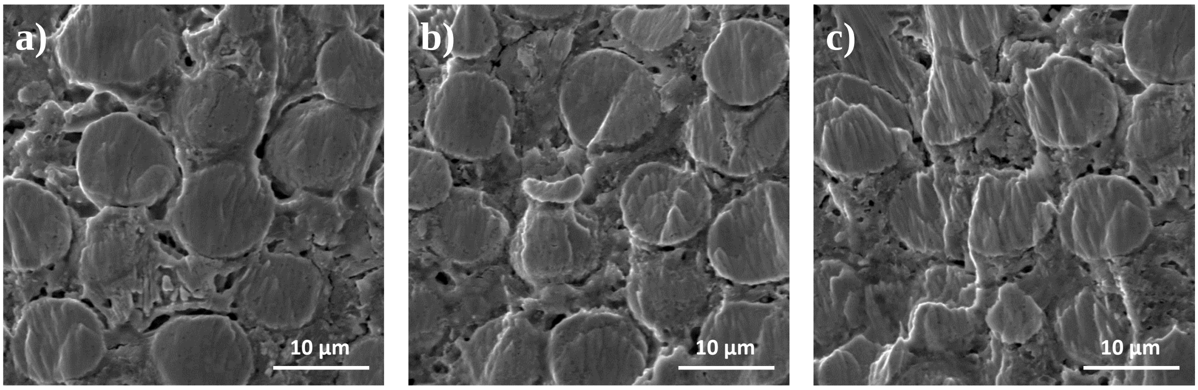

Figure S14. Cross-sectional SEM images of (a) AP-NMC, (b) SCP-NMC, and (c) CP-NMC after 25 cycles.